



Visible light $\text{Bi}_2\text{S}_3/\text{Bi}_2\text{O}_3/\text{Bi}_2\text{O}_2\text{CO}_3$ photocatalyst for effective degradation of organic pollutions

Yongchao Huang ^a, Wenjie Fan ^a, Bei Long ^a, Haibo Li ^a, Fengyi Zhao ^a, Zili Liu ^b,
Yexiang Tong ^{a,*}, Hongbing Ji ^{a, **}

^a MOE of the Key Laboratory of Bioinorganic and Synthetic Chemistry, KLGHEI of Environment and Energy Chemistry, The Key Lab of Low-carbon Chem & Energy Conservation of Guangdong Province, Sun Yat-Sen University, 135 Xingang West Road, Guangzhou 510275, PR China

^b Guangzhou University, School of Chemistry and Chemical Engineering, Guangzhou, PR China

ARTICLE INFO

Article history:

Received 12 October 2015

Received in revised form

24 November 2015

Accepted 27 November 2015

Available online 1 December 2015

Keywords:

$\text{Bi}_2\text{S}_3/\text{Bi}_2\text{O}_3/\text{Bi}_2\text{O}_2\text{CO}_3$

Photocatalysis

Electron-hole separation

Environmental remediation

ABSTRACT

$\text{Bi}_2\text{S}_3/\text{Bi}_2\text{O}_3/\text{Bi}_2\text{O}_2\text{CO}_3$ photocatalyst was successfully synthesized by combining the rational heat-treatment process and ion exchange technique. These composites exhibited superior photocatalytic activities for organic contaminants (formaldehyde gas, methyl orange and phenol) degradation under the visible light irradiation. These catalysts could eliminate more than 99% of formaldehyde gas within 100 min, which is considerably higher than those of pure $\text{Bi}_2\text{O}_2\text{CO}_3$ (10.9%) and $\text{Bi}_2\text{O}_3/\text{Bi}_2\text{O}_2\text{CO}_3$ (23.6%) samples at the same condition. Furthermore, these as-prepared $\text{Bi}_2\text{S}_3/\text{Bi}_2\text{O}_3/\text{Bi}_2\text{O}_2\text{CO}_3$ composites also show excellent photocatalytic performance for methyl orange and phenol removing as well as good stability. The highly improved performance of the composites can be ascribed to the increased light absorption and efficient charge separation. In addition, the photocatalytic process is mainly governed by the super-oxide and the holes rather than the hydroxyl radicals. These features suggest the current heterostructured photocatalysts can be applied in environmental remediation and waste water treatment.

© 2015 Elsevier B.V. All rights reserved.

1. Introduction

Semiconductor-based photocatalysis has attracted much attention as a potential solution for dealing with global energy crisis and environmental pollution [1–4]. Recently, considerable attention has been drawn to the bismuth-based semiconductors [5–9]. It has been found that many Bi-based compounds possess a narrow band gap and exhibit high visible-light photocatalytic activity because of their hybridized O 2p and Bi 6s² valence bands [10,11]. Bismuth subcarbonate ($\text{Bi}_2\text{O}_2\text{CO}_3$) is one of the most attractive photocatalysts for the degradation of organic dyes and low mammalian toxicity for medicine treatment [12–14]. However, $\text{Bi}_2\text{O}_2\text{CO}_3$ photocatalysts solely absorb UV light due to their wide band gap, which greatly limits their practical applications. On the other hand, the photocatalytic efficiency of $\text{Bi}_2\text{O}_2\text{CO}_3$ photocatalysts is also usually limited by the ability of separation and/or combination of photo-generated electron–hole pairs. Therefore, it is necessary to develop an effective strategy to improve charge separation efficiency and

enhance visible light responsive activity of the $\text{Bi}_2\text{O}_2\text{CO}_3$ photocatalyst.

Up to date, a variety of attempts have been investigated to enhance the photocatalytic performance of $\text{Bi}_2\text{O}_2\text{CO}_3$, such as: doping [15–17], morphology tuning to shorten the transfer distance of minority carriers [18], and coupling with smaller band gap semiconductors [19,20]. Especially, a heterojunction photocatalyst containing two or more different semiconductors offers more promising advantages in photocatalytic system, which can not only improve light absorption ability due to the narrow band gap semiconductor, but also provide efficient charge separation efficiency because of their appropriate band-gap position. Recently, $\text{Bi}_2\text{O}_2\text{CO}_3/\text{Bi}_2\text{O}_3$ heterojunction has been taken considerable attention because it uses more visible light and effectively suppresses photogenerated electron–hole recombination. For example, Cai et al. prepared $\beta\text{-Bi}_2\text{O}_3/\text{Bi}_2\text{O}_2\text{CO}_3$ nanocomposite via a rational heat-treatment of $\text{Bi}_2\text{O}_2\text{CO}_3$ precursor and it was found that $\text{Bi}_2\text{O}_3/\text{Bi}_2\text{O}_2\text{CO}_3$ photocatalyst displayed much higher photocatalytic performance for the degradation of methylene blue than pure $\text{Bi}_2\text{O}_2\text{CO}_3$ and Bi_2O_3 under visible light [21]. And Hu et al. improved the photocatalytic performance of the $\text{Bi}_2\text{O}_3/\text{Bi}_2\text{O}_2\text{CO}_3$ due to the formation of p-n junction with large heterojunction interface. And this p-n heterojunction structure could effectively

* Corresponding author.

** Corresponding author.

E-mail addresses: chedhx@mail.sysu.edu.cn (Y. Tong), jihb@mail.sysu.edu.cn (H. Ji).

enhance the separation of photo-generated electron-hole pairs, which will further enhance its photocatalytic performance [22]. This result indicates that tailoring and fabricating of the phase interface/junctions between the light harvesting semiconductors could be effective in improving the photocatalytic activity and stability. However, the absorption and the charge transfer rate of $\text{Bi}_2\text{O}_3/\text{Bi}_2\text{O}_2\text{CO}_3$ heterojunction involved in the process still need to be improved.

Coupling with smaller band gap semiconductors is considered to be an effective progress to enhance the photocatalytic performance [10,23–26]. With coupling nanoscale low-bandgap semiconductor, it can be expected that the photocatalytic activity of $\text{Bi}_2\text{O}_3/\text{Bi}_2\text{O}_2\text{CO}_3$ heterojunction will be significantly improved by the enhancement of charge separation and photoabsorption. As an important chalcogenide compound, bismuth sulfide (Bi_2S_3) is a promising photocatalyst and attracts more and more attention due to its photosensitization in the visible region, which makes Bi_2S_3 an effective semiconductor material for photocatalytic applications [27,28]. Furthermore, ion exchange chemistry has been showed to be an effective method for transforming performed nanocrystals templates into more complex heterostructures, such as core-shell nanoparticles, providing additional levers for tuning material properties [29–31]. To the best of our knowledge, the synthesis and application of the structure of $\text{Bi}_2\text{S}_3/\text{Bi}_2\text{O}_3/\text{Bi}_2\text{O}_2\text{CO}_3$ heterojunction have not been reported. In this work, we synthesized the $\text{Bi}_2\text{S}_3/\text{Bi}_2\text{O}_3/\text{Bi}_2\text{O}_2\text{CO}_3$ heterojunction via simple phase transformation and cation exchange route. The obtained $\text{Bi}_2\text{S}_3/\text{Bi}_2\text{O}_3/\text{Bi}_2\text{O}_2\text{CO}_3$ heterojunction photocatalyst exhibits extremely high activity and stability, which is ascribed to the increased light absorption and efficient charge separation.

2. Experimental

2.1. Preparation of catalysts

In a typical synthesis process, sodium carbonate (0.46 g) was first dissolved in distilled water (70 mL) in a 100 mL autoclaved Teflon vessel and the mixture was then stirred for 10 min. Afterward, bismuth citrate (1.6 g) was added to the solution, and the mixture was stirred for 30 min to ensure that all reagents were dissolved. The resulting precursor suspension was hydrothermally treated at 160 °C for 24 h. After the mixture was cooled to room temperature, the resulting solid was filtered, washed with water and ethanol four times, and dried at 60 °C for 12 h to obtain the $\text{Bi}_2\text{O}_2\text{CO}_3$ (BOC) sample. To obtain the $\text{Bi}_2\text{O}_3/\text{BOC}$ heterostructures, the BOC (0.2 g) was annealed at different temperature in air for 2 h. and then $\text{Bi}_2\text{O}_3/\text{BOC}$ heterostructures (0.2 g) were immersed in Na_2S solution (0.05 M) for different time to obtain $\text{Bi}_2\text{S}_3/\text{Bi}_2\text{O}_3/\text{BOC}$ samples. The samples were filtered, washed with water and ethanol four times, and dried at 60 °C for 12 h.

2.2. Characterization

The samples were characterized by X-ray Diffractometer (XRD, D8 ADVANCE), field emission scanning electron microscope (FE-SEM, JSM-6330 F), Transmission electron microscopy (TEM, JEM2010-HR) and X-ray photoelectron spectroscopy (XPS, ESCALab250). Fourier-transform infrared (FTIR) spectra were collected on a Nicolet Avatar 370 infrared spectrometer in the range of 500–4000 cm^{-1} using pressed KBr discs. UV–vis diffuse reflectance spectra (DRS) of the samples were recorded on a UV–vis spectrophotometer (UV-2450) with an integrating sphere attachment within the range of 230–800 nm and with BaSO_4 as the reflectance standard. The photoluminescence spectrometer under the ultraviolet excitation of 400 nm. The specific surface was calculated using

the Brunauer–Emmett–Teller (BET) method using the measurement instrument (ASAP 2020 V3.03 H). Electron spin resonance (ESR) tests were carried out in the X-band (9.45 GHZ) with 5.00 G modulation amplitude and a magnetic field modulation of 100 kHz using a Bruker, A300-10-12 Bruker ESP spectrometer at 77 K. Photocurrent measurement was tested with a CHI 660C electrochemical station in a standard three electrode configuration, samples as the working electrodes, a platinum plate as the counter electrode, and a Ag/AgCl electrode as the reference electrode. A 0.5 mol/L Na_2SO_4 aqueous solution was used as the electrolyte. A 300 W Xe lamp with a 420 nm UV light cut filter was used as the visible light source and the light intensity is 100 mW cm^{-2} .

2.3. Photocatalytic activity measurements

The photocatalytic activity of the as-synthesized samples (0.1 g) was first evaluated by removing HCHO at 500 ppm in a closed reactor. The reactor had a capacity of 4.5 L (30 cm × 15 cm × 10 cm), made of polymeric glass and covered with Saint-Glass. A tungsten halogen lamp (100 W) with a 420 nm UV light cut filter was vertically placed 20 cm above the reactor under the condition of constant temperature at 25 °C. The products of the reaction were analyzed online by an Agilent 7890A gas chromatograph with a TCD detector and a Porapak-Q column. Only CO_2 in the products were detected for all the tested catalysts. The HCHO conversion was calculated from the CO_2 content as follows:

$$\text{HCHO conversion}(\%) = \frac{[\text{CO}_2]_{\text{out}}}{[\text{HCHO}]_{\text{in}}} \times 100$$

$[\text{CO}_2]_{\text{out}}$ and $[\text{HCHO}]_{\text{in}}$ in the formula are the CO_2 concentration in the products and the HCHO concentration in the reactor, respectively.

A certain amount of the catalyst (50 mg) was added to a 100 mL reaction solution containing MO (20 mg/L) or phenol (10 mg/L). The solution with catalysts was magnetically stirred for 90 min in dark and then the solution can establish absorption–desorption equilibrium. A 500 W Xe lamp was used as the visible light source with a 420 nm UV light cut filter. The light intensity of our photocatalytic tests is 100 mW cm^{-2} . After the light irradiation, the reactive solution (3.0 mL) was taken out by the syringe at different time. The residual dyes concentration was tested by UV–vis spectrophotometry. For MO system, the residual MO concentration was calculated with the intensity of the 465 nm absorbance. For phenol system, the residual phenol was calculated on the 270 nm absorbance. The photocatalytic efficiency was calculated by the $\text{C}/\text{C}_0 \times 100\%$, where the C is the final dyes concentration, C_0 is the initial concentration of dyes.

3. Results and discussion

3.1. Structure and composition of catalysts

In the preparation of the catalysts, $\text{Bi}_2\text{O}_2\text{CO}_3$ (BOC) was first synthesized by a simple hydrothermal method (details in the Experimental Methods). In order to determine the temperatures for phase transformation of BOC, thermo gravimetric analysis (TGA) was carried out. Fig. S1 shows the BOC decomposes thermally to Bi_2O_3 . At the temperature of 240 °C, the BOC phase begins to transform to Bi_2O_3 : $\text{Bi}_2\text{O}_2\text{CO}_3 \rightarrow \text{Bi}_2\text{O}_3 + \text{CO}_2$. After the 350 °C, the weight loss is not observed, which suggests that Bi_2O_3 is stable. Thus, the $\text{Bi}_2\text{O}_3/\text{BOC}$ nanocomposite can be obtained via a rational heat-treatment of BOC precursor. To obtain the $\text{Bi}_2\text{O}_3/\text{BOC}$ heterostructures, the BOC was annealed at different temperature in air. And $\text{Bi}_2\text{S}_3/\text{Bi}_2\text{O}_3/\text{BOC}$ heterojunction was obtained through an anion exchange method with Na_2S solution at different time.

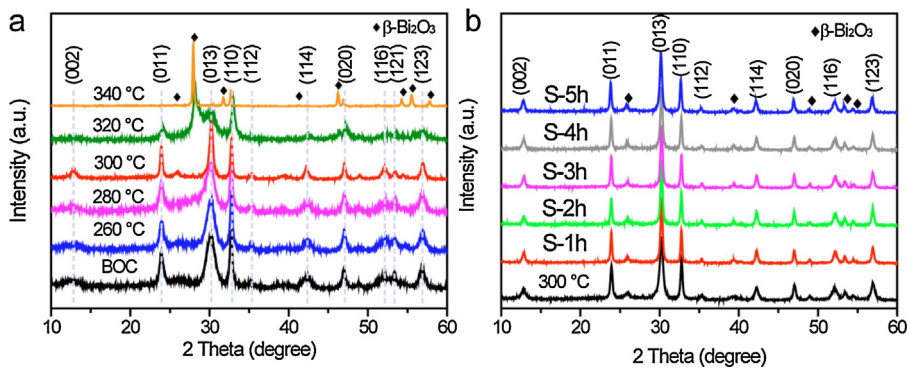


Fig. 1. XRD patterns of the samples (a) calcined at different temperatures and (b) anion exchange with different time.

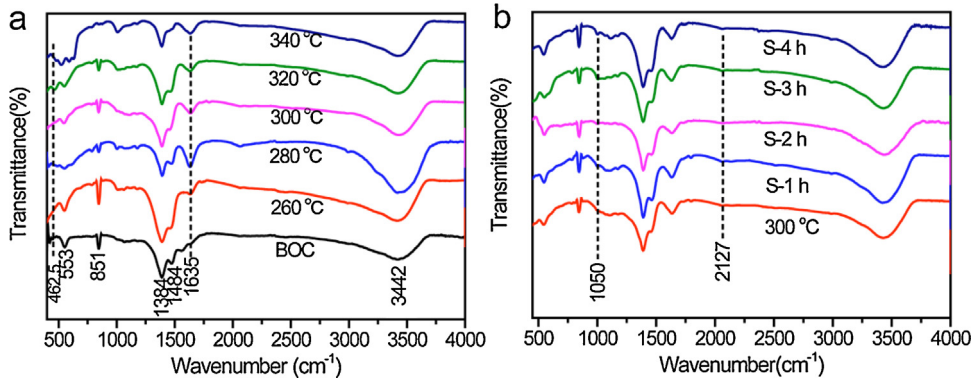


Fig. 2. FT-IR spectra of the samples (a) calcined at different temperatures and (b) anion exchange with different time.

The crystal quality of the as-synthesized samples were analyzed by X-ray diffraction (XRD) as showed in Fig. 1. All patterns of samples exhibit sharp diffraction peaks, indicating that all samples were highly crystalline. Fig. 1a shows the XRD patterns of BOC before and after heat treatment. It can be seen that BOC exhibits a tetragonal crystal structure (PCPDS No.42-1488). And the diffraction patterns remained consistent with the pure BOC phase as the calcination temperature up to 280 °C. After the temperature reached 300 °C, tetragonal β -Bi₂O₃ appeared, which matched well with values from the standard card (JCPDS No.27-0050). From 280 to 340 °C, the diffraction peaks of BOC gradually decreased, while the peaks of β -Bi₂O₃ phase were simultaneously enhanced, which suggesting that the formation of Bi₂O₃/BOC composites. Highly pure β -Bi₂O₃ samples were obtained as the temperature was increased from 340 °C. However, after anion exchange of Bi₂O₃/BOC with different time, the diffraction peaks did not changed, which suggesting that the peak for Bi₂S₃ cannot be detected may be due to Bi₂S₃ particles were amorphous structure (Fig. 1b).

FT-IR spectroscopy and Raman spectrum were carried out to further confirm the composition of samples and analyze the chemical interaction between Bi₂O₃ and Bi₂S₃. Fig. 2 shows the FT-IR spectra of all the prepared samples. The absorption bands at 541 cm⁻¹ and 851 cm⁻¹ for BOC and Bi₂O₃/BOC were attributed to the stretching mode of the Bi–O while the peaks about 1384 cm⁻¹ and 1484 cm⁻¹ were assigned to the stretching vibrations of C=O [32]. The broad band at 3442 cm⁻¹ can be due to the stretching mode of O–H. For Bi₂S₃/Bi₂O₃/BOC samples, two new weak peaks (1050 cm⁻¹, 2127 cm⁻¹) generated due to the formation of Bi₂S₃ [33]. Furthermore, Raman spectra of the BOC, Bi₂O₃/BOC and Bi₂S₃/Bi₂O₃/BOC were showed in Fig. S2. The Raman spectra of BOC and Bi₂O₃/BOC exhibit a peak corresponding to the Raman shift of 163 cm⁻¹, which is ascribed to the vibration modes of the carbonate ion [34]. While the Raman spectra of Bi₂S₃/Bi₂O₃/BOC appeared a new peak at

239 cm⁻¹ due to the formation of Bi₂S₃ [35]. All above results demonstrated the successful combination of the Bi₂O₃/BOC and Bi₂S₃/Bi₂O₃/BOC heterojunction.

The X-ray photoelectron spectroscopy (XPS) was carried out to further illuminate the chemical states and the compositions existent in the BOC, Bi₂O₃/BOC and Bi₂S₃/Bi₂O₃/BOC catalysts. Fig. S3 shows the survey spectrum of the samples, which reveals the samples possess Bi, O and C elements. Fig. 3a shows the Bi 4f spectra of the BOC, Bi₂O₃/BOC and Bi₂S₃/Bi₂O₃/BOC catalysts. There are two strong peaks at 158.9 eV and 164.3 eV, which are assigned to Bi 4f_{7/2} and Bi 4f_{5/2} and corresponded to Bi³⁺ [6,36]. Moreover, the XPS results of O 1s signals are showed in Fig. 3b, there are two major peaks at 530.7 and 534.9 eV. The obvious peak at 530.7 eV is the characterization of Bi–O bonds [37]. However, the peak at 534.9 eV is different for BOC, Bi₂O₃/BOC and Bi₂S₃/Bi₂O₃/BOC catalysts, which reveals that the interfacial structures have some change after annealed and ion exchange. In addition, Fig. 3c displays the core level spectrum of C 1s of BOC, Bi₂O₃/BOC and Bi₂S₃/Bi₂O₃/BOC catalysts, which can be fitted with two dominant peaks. The peak at 284.9 eV is due to the adventitious carbon species and the other at 288.8 eV can be assigned to the carbonate ion in BOC. Note that only the S 2s can be detected in Bi₂S₃/Bi₂O₃/BOC heterojunction (Fig. 3d). These results indicate the presence of Bi₂S₃, implying the formation of Bi₂S₃/Bi₂O₃/BOC heterojunction.

3.2. Morphology analysis

The scanning electron microscopy (SEM) images reveal that BOC samples consist of many flowerlike hierarchical microspheres ($\sim 1.0 \mu\text{m}$) self-assembled by nanosheets (Fig. 4a). However, SEM studies reveal that there is no obvious morphological change in nanosheet structure upon thermal treatment and anion exchange (Fig. 4b and c). The detailed structural information of the sam-

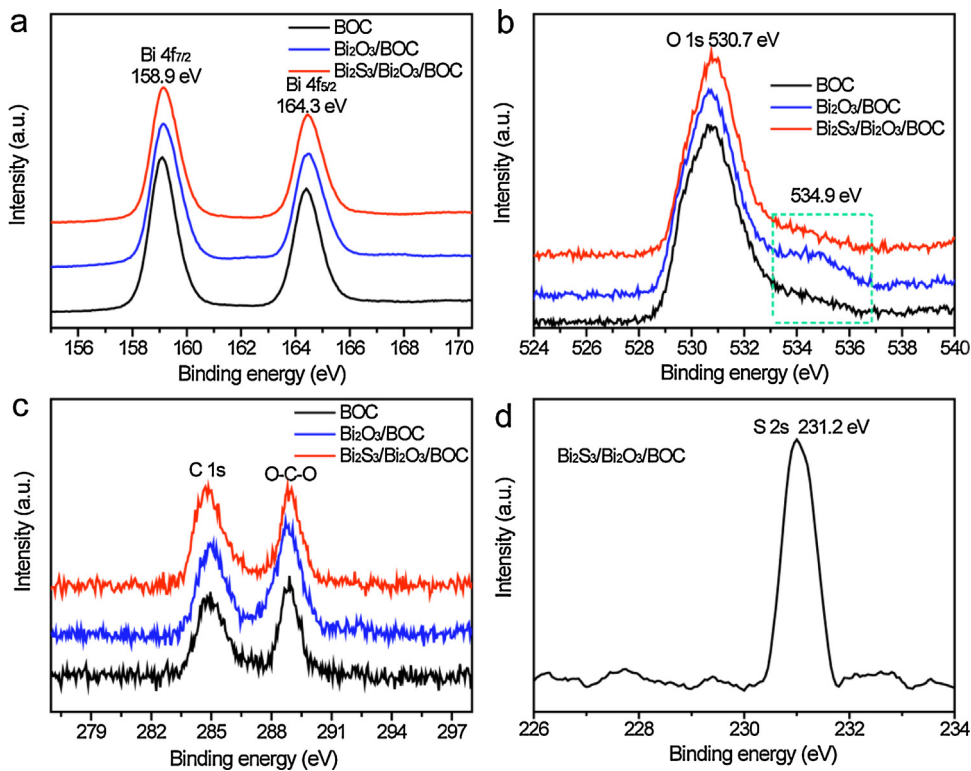


Fig. 3. (a) Normalized core-level Bi 4f, (b) normalized core-level O 1s, and (c) normalized core-level C 1s XPS spectra for BOC, $\text{Bi}_2\text{O}_3/\text{BOC}$ and $\text{Bi}_2\text{S}_3/\text{Bi}_2\text{O}_3/\text{BOC}$. (d) Normalized core-level S 2s XPS spectra for $\text{Bi}_2\text{S}_3/\text{Bi}_2\text{O}_3/\text{BOC}$.

amples were further studied by transmission electron microscopy (TEM). The TEM image (Fig. 4d) reveals that the BOC has a diameter of $1.0\text{ }\mu\text{m}$ with microsphere-like appearance, which is in good agreement with the size and shape of SEM observed. And these microspheres are composed of numerous nanosheets. When BOC was calcined at $300\text{ }^\circ\text{C}$, the microsphere showed some changes in morphology, which was caused by the partial decomposition of BOC and formation of Bi_2O_3 . Fig. 4g–i displayed the high-resolution TEM (HRTEM) images of BOC, $\text{Bi}_2\text{O}_3/\text{BOC}$ and $\text{Bi}_2\text{S}_3/\text{Bi}_2\text{O}_3/\text{BOC}$, respectively. For BOC, there are only obvious lattice fringes of BOC, and the resolved interplanar distance is 0.292 nm , which was the (013) plane of BOC. After annealed, some clear fringes of Bi_2O_3 nanocrystals are detected (Fig. 4H) and the resolved interplanar distance of 0.327 nm and 0.292 nm are corresponding to (3 1 0) plane of Bi_2O_3 and (0 1 3) plane of BOC, suggesting that Bi_2O_3 phase was formed over BOC. These results suggest that the $\text{Bi}_2\text{O}_3/\text{BOC}$ samples could be obtained by annealing the BOC. After anion exchange with Na_2S , there are some small particles on the surfaces of $\text{Bi}_2\text{O}_3/\text{BOC}$, which obviously reveal that the Bi_2S_3 was formed. Selected-area electron diffraction (SAED) analyses show that the Bi_2S_3 is amorphous structure, which corresponds to the XRD of Bi_2S_3 . These results above showed that the successful fabrication of $\text{Bi}_2\text{S}_3/\text{Bi}_2\text{O}_3/\text{BOC}$ heterojunction.

3.3. Photocatalytic activity test

In order to study the photocatalytic performance of all the catalysts, photodegradation of HCHO gas (one of the indoor pollutions) [38,39] as well as water pollutions (methyl orange (MO) (pH 9), and phenol) were carried out under visible light irradiation. All the samples were magnetically stirred in the dark to study the absorption capabilities of HCHO and MO. Fig. 5a shows the HCHO adsorption capabilities of all the samples. After 60 min, the BOC catalyst has the highest absorption capability, which was because

the specific surface area of BOC ($64.97\text{ m}^2\text{ g}^{-1}$) is larger than that of $\text{Bi}_2\text{O}_3/\text{BOC}$ ($35.79\text{ m}^2\text{ g}^{-1}$) and $\text{Bi}_2\text{S}_3/\text{Bi}_2\text{O}_3/\text{BOC}$ ($36.74\text{ m}^2\text{ g}^{-1}$) (Fig. S4). There is the same case for the MO absorption capability, which was showed in Fig. 5b. Fig. 5c displays the photocatalytic performance of HCHO degradation with different catalysts under visible light irradiation. $\text{Bi}_2\text{S}_3/\text{Bi}_2\text{O}_3/\text{BOC}$ catalyst exhibits the highest catalytic performance of HCHO oxidation, which could remove 99% HCHO in 100 min. While there are only 24% for $\text{Bi}_2\text{O}_3/\text{BOC}$ and 11.2% for BOC, respectively, suggesting that $\text{Bi}_2\text{S}_3/\text{Bi}_2\text{O}_3/\text{BOC}$ catalyst has the superior photocatalytic activity under visible light. Furthermore, Fig. 5d shows that MO can only be slightly degraded under visible light irradiation without catalysts, indicating that MO is a stable molecule and that the photolysis mechanism can be ignored. At the same condition, P25 as the catalyst shows that the dye photosensitization process is not obvious (Fig. S5). Therefore, the dye photosensitization process can be ignored in our experiments. Fig. 5d and S6 also reveals that the $\text{Bi}_2\text{S}_3/\text{Bi}_2\text{O}_3/\text{BOC}$ samples exhibit excellent photocatalytic performances for the MO degradation. $\text{Bi}_2\text{S}_3/\text{Bi}_2\text{O}_3/\text{BOC}$ heterojunction shows extremely high photocatalytic activity and could completely degrade MO in 60 min under visible light irradiation. While there are only 44% MO for $\text{Bi}_2\text{O}_3/\text{BOC}$ and 20% MO for BOC could be decompose with the same condition. The pseudo-first-order rate constants (Fig. S6c) over BOC, $\text{Bi}_2\text{O}_3/\text{BOC}$, $\text{Bi}_2\text{S}_3/\text{BOC}$, and $\text{Bi}_2\text{S}_3/\text{Bi}_2\text{O}_3/\text{BOC}$ are 0.0022 , 0.0114 , 0.0145 , and 0.0494 min^{-1} , respectively. Moreover, Fig. 5e shows that in degradation of phenol, $\text{Bi}_2\text{S}_3/\text{Bi}_2\text{O}_3/\text{BOC}$ also exhibits more efficiency than $\text{Bi}_2\text{O}_2\text{CO}_3$, $\text{Bi}_2\text{O}_3/\text{BOC}$, and $\text{Bi}_2\text{S}_3/\text{BOC}$. All these results convincingly demonstrate that the $\text{Bi}_2\text{S}_3/\text{Bi}_2\text{O}_3/\text{BOC}$ has the superior photocatalytic activity under visible light. More importantly, Fig. 5f shows that very high stability was obtained over the $\text{Bi}_2\text{S}_3/\text{Bi}_2\text{O}_3/\text{BOC}$ heterostructured photocatalyst. Notably, even after 5 successive cycles, $\text{Bi}_2\text{S}_3/\text{Bi}_2\text{O}_3/\text{BOC}$ still could degrade 96% MO under visible light irradiation, suggesting the high stability of $\text{Bi}_2\text{S}_3/\text{Bi}_2\text{O}_3/\text{BOC}$. In addition to the advantage in such efficiency,

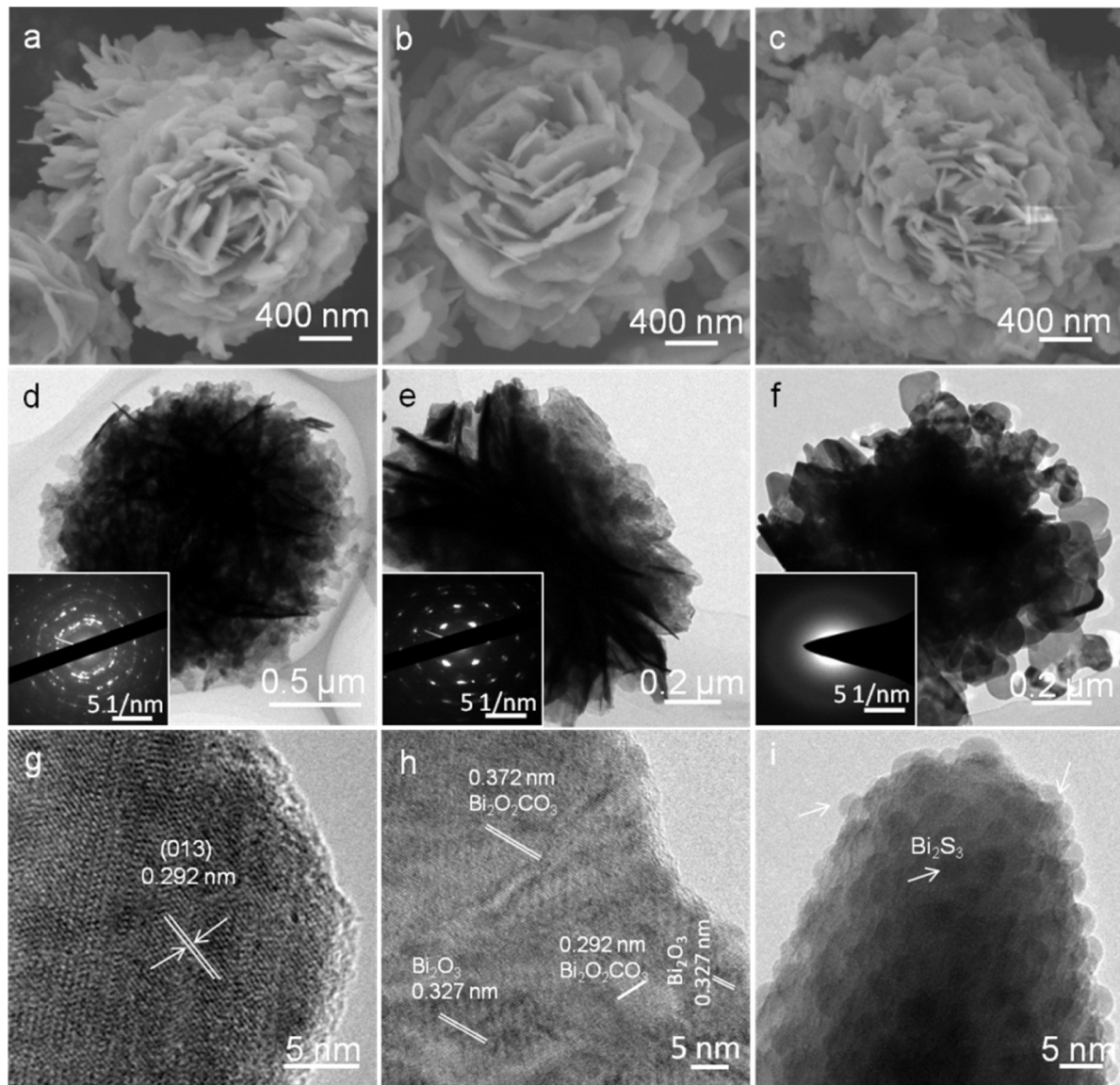


Fig. 4. SEM images of BOC (a), Bi_2O_3 /BOC (b), Bi_2S_3 / Bi_2O_3 /BOC (c). TEM images of BOC (d), Bi_2O_3 /BOC (e), Bi_2S_3 / Bi_2O_3 /BOC (f). And high-resolution TEM images of BOC (g), Bi_2O_3 /BOC (h), Bi_2S_3 / Bi_2O_3 /BOC (i).

the Bi_2S_3 / Bi_2O_3 /BOC exhibits excellent performance stability, with strong resistance to morphology and composition changes (Fig. S7).

3.4. Light absorption, charge separation, and photoluminescence analysis

The photocatalytic performance obtained with Bi_2S_3 / Bi_2O_3 /BOC catalyst in this study is comparable or better than most of the catalysts reported in the literature (Table S1). The good efficiency of Bi_2S_3 / Bi_2O_3 /BOC nanostructure catalyst may be attributed to two factors. First, the improved light-harvesting ability is believed to be one major reason for the superior photocatalytic activity of Bi_2S_3 / Bi_2O_3 /BOC heterojunction. Fig. 6a shows the UV-vis absorption spectra of BOC, Bi_2O_3 /BOC and Bi_2S_3 / Bi_2O_3 /BOC samples. BOC sample has an edge around 383 nm. Due to its wide bandgap (3.3 eV), the BOC has no obvious absorbance in the visible light region. The maximal absorbance wavelength of Bi_2O_3 /BOC sample is approximately 450 nm. While after Bi_2S_3 / Bi_2O_3 /BOC heterojunction being formed, the optical absorption increases in the visible light region, and the band gap is to be 1.32 eV. Correspondingly, the materials display different colors ranging from beige white to gray

(inset of Fig. S1). This supports that the introduction of Bi_2S_3 can intrinsically improve the optical absorption property of Bi_2O_3 /BOC. Second, the charge separation and migration should significantly affect the photocatalytic performance, which can be verified in the photocurrent response experiment [40]. As shown in Fig. 6b, the Bi_2S_3 / Bi_2O_3 /BOC heterojunction displays the largest photocurrent density, which confirms the intrinsic advantages of this structure in facilitating the separation of the photogenerated carriers.

Photoluminescence spectra are usually used to explore the efficiency of the charge carrier trapping, migration, and transfer, and it is quite helpful to understand the fate of electron-hole pairs in semiconductor as PL emission arises from the recombination of free carriers [41]. A low PL intensity is generally indicative of a high separation efficiency of electron-hole pairs. Fig. 6c shows the PL spectra of the BOC, Bi_2O_3 /BOC and Bi_2S_3 / Bi_2O_3 /BOC heterostructures. The BOC samples exhibit a broad emission peak centered around 450–600 nm. Obviously, the Bi_2S_3 / Bi_2O_3 /BOC heterostructures show significantly diminished PL intensity in comparison with BOC and Bi_2O_3 /BOC, which suggests that it possesses the highest separation efficiency of charge carriers. Furthermore, Fig. 6d displays the electrochemical impedance spectroscopy (EIS) of BOC,

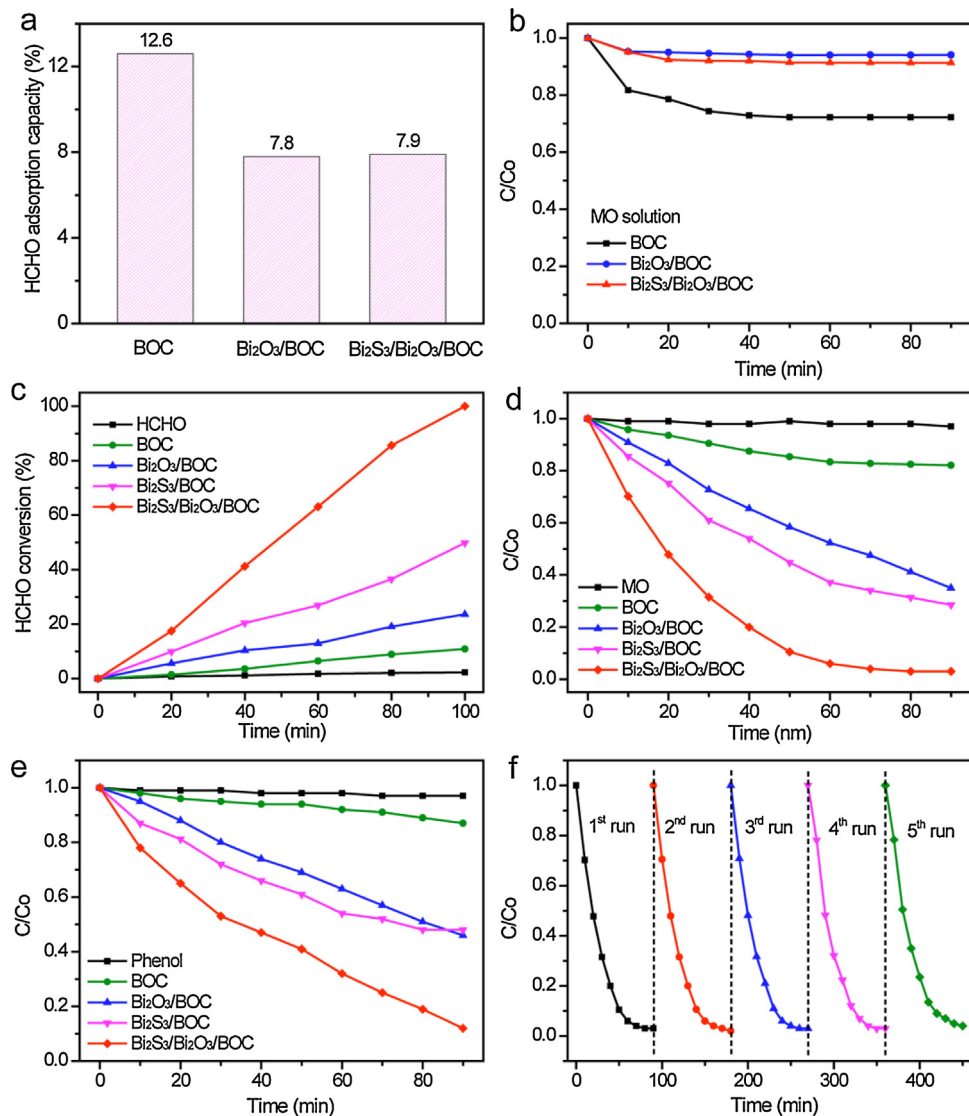


Fig. 5. (a) HCHO adsorption capacity of BOC, Bi₂O₃/BOC and Bi₂S₃/Bi₂O₃/BOC. (b) In darkness, MO aqueous solution under photocatalysis using as-prepared samples as a function of time. Photocatalytic activity of as-prepared samples for degradation of (c) HCHO, (d) MO and (e) phenol under visible light irradiation. (f) Cycling performance of photocatalytic degradation of MO over Bi₂S₃/Bi₂O₃/BOC samples.

Bi₂O₃/BOC and Bi₂S₃/Bi₂O₃/BOC heterostructures, revealing the photogenerated charge carried behaviors. It is known that the reaction rate occurring at the surface of the electrodes can be revealed by the arc radius on the EIS Nyquist plot [42]. The diameter of the arc radius of BOC, Bi₂O₃/BOC and Bi₂S₃/Bi₂O₃/BOC under light irradiation are smaller than those in the darkness, revealing that the photoexcited carries have generated. More importantly, the Bi₂S₃/Bi₂O₃/BOC has the smallest diameter of the arc radius, suggesting the effective separation of photogenerated carriers over Bi₂S₃/Bi₂O₃/BOC.

3.5. Reaction mechanisms

To explore the mechanism of the high photocatalytic activity, we first carried out trapping experiments of reactive species in this photocatalytic process. Three different quenchers, benzoquinone (BQ; a O₂^{•-} radical scavenger), tert-butylalcohol (TBA; a OH radical scavenger), and triethanolamine (TEOA; a h⁺ scavenger) were used [43]. The experimental results (Fig. S8) show that the addition of BQ or TEOA caused obviously deactivation of the Bi₂S₃/Bi₂O₃/BOC photocatalyst, reducing the photocatalytic activity for the degradation

rate of MO from 100% to 60% (TEOA) and 40% (BQ). The possible reason is that the addition of BQ to the photocatalytic system results in the capture of O₂^{•-} by BQ and the decrease in the amount of active O₂^{•-} radicals for photocatalytic reactions. As for TEOA, which can be adsorbed on the surface of the photocatalyst and can act as a hole trap, resulting the deactivation of the Bi₂S₃/Bi₂O₃/BOC photocatalyst. To further confirm these conclusion, we performed the electron spin resonance (ESR) spectroscopy to detect •OH and O₂^{•-} production. As shown in Fig. 7a, no signal of •OH was detected in the system containing Bi₂S₃/Bi₂O₃/BOC under visible light irradiation, which suggests that •OH oxidation is not the main reaction during photocatalytic process. As indicated in Fig. 7b, six apparent signals were generated, which were attributed to DMPO-•O₂^{•-} with the Bi₂S₃/Bi₂O₃/BOC in methanol under visible light irradiation for 20 min, while no •O₂^{•-} signal was detected in dark under otherwise identical condition. Based on the above results, the photocatalytic process is mainly governed by the superoxide and the holes rather than the hydroxyl radicals. However, the redox potential of O₂/•O₂^{•-} is -0.33 eV, which is more negative than that of the CB of BOC and Bi₂O₃, the CB electrons could not reduce the O₂. We detected that there are some superoxide generation, which only

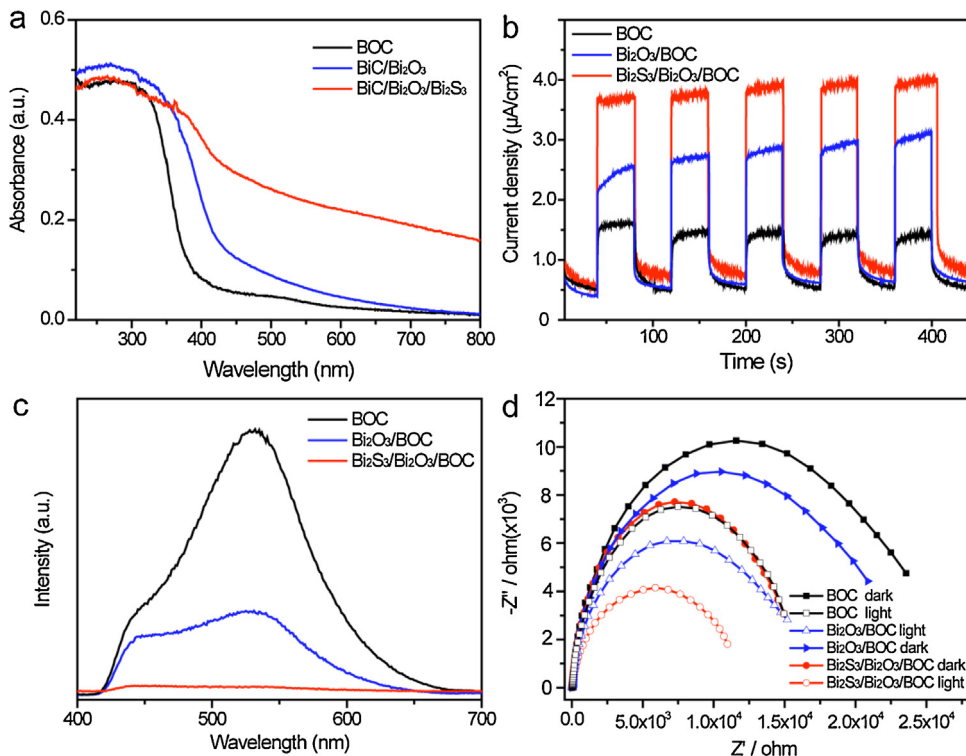


Fig. 6. (a) UV–vis absorption spectra of BOC, $\text{Bi}_2\text{O}_3/\text{BOC}$ and $\text{Bi}_2\text{S}_3/\text{Bi}_2\text{O}_3/\text{BOC}$. (b) Photocurrent responses of BOC, $\text{Bi}_2\text{O}_3/\text{BOC}$ and $\text{Bi}_2\text{S}_3/\text{Bi}_2\text{O}_3/\text{BOC}$ samples measured at the bias of 0.1 V versus Ag/AgCl under visible light irradiation. (c) Photoluminescence spectra of BOC, $\text{Bi}_2\text{O}_3/\text{BOC}$ and $\text{Bi}_2\text{S}_3/\text{Bi}_2\text{O}_3/\text{BOC}$ samples with an excitation wavelength of 400 nm. (d) EIS spectra of BOC, $\text{Bi}_2\text{O}_3/\text{BOC}$ and $\text{Bi}_2\text{S}_3/\text{Bi}_2\text{O}_3/\text{BOC}$ samples in the darkness and under visible light irradiation.

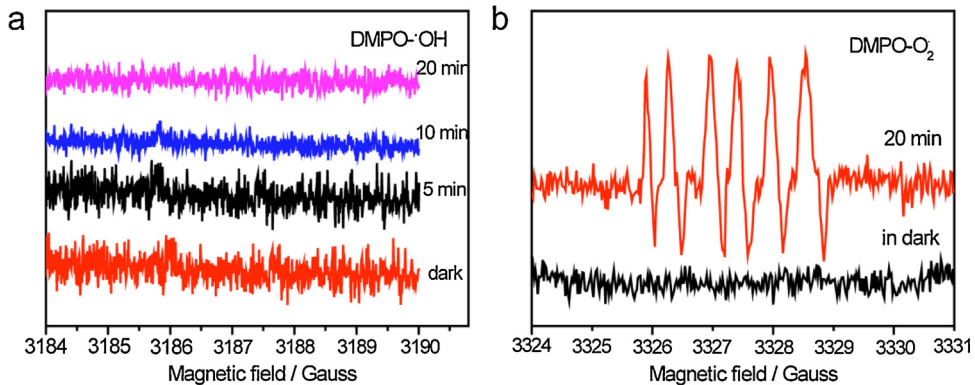


Fig. 7. DMPO spin-trapping ESR spectra recorded at ambient temperature in aqueous $\text{Bi}_2\text{S}_3/\text{Bi}_2\text{O}_3/\text{BOC}$ dispersion for DMPO- $\cdot\text{OH}$ (a), as well as in CH_3OH dispersion for DMPO- O_2^- (b) under visible irradiation (>420 nm). The settings for the ESR spectrometer were as follows: center field, 3367 G; sweep width, 80 G; microwave frequency, 9.44 GHz; modulation frequency, 100 kHz and power, 0.998 mW.

can generate by Bi_2S_3 . It mean that some electrons reacted with the O_2 and most migrated to the CBM of BOC and Bi_2O_3 . The photo-generated holes moved and gathered to the VBM of Bi_2S_3 , which can directly oxidized the dyes.

The band gap energy (E_g) was evaluated using the following equation:

$$\alpha(hv) = A(hv - E_g)^{n/2}$$

Where α , v , E_g , and A are the absorption coefficient, light frequency, band gap energy, and a constant, respectively, and n is determined by the type of optical transition in the semiconductor. The band gap energies (E_g) of these samples were estimated from a plot of $(\alpha h\nu)^{1/2}$ as a function of the photon energy ($h\nu$) to be approximately 3.30, 2.35, and 1.32 eV for $\text{Bi}_2\text{O}_2\text{CO}_3$, Bi_2O_3 , and Bi_2S_3 , respectively. The band positions of the as-synthesized $\text{Bi}_2\text{O}_2\text{CO}_3$, Bi_2O_3 , and Bi_2S_3 were calculated using the following empirical

equation: $E_{\text{VB}} = X - E^e + 0.5E_g$, where E_{VB} is the valence band edge potentials, X is the electronegativity of the semiconductor, E^e is the energy of the free electrons on the hydrogen scale (approximately 4.5 eV), E_g is the band gap energy of the semiconductor. The E_{CB} (conductance band edge potentials) can be calculated using the following equation $E_{\text{CB}} = E_{\text{VB}} - E_g$. The results were showed in Table S2. From the above results the possible charge transfer process over $\text{Bi}_2\text{S}_3/\text{Bi}_2\text{O}_3/\text{BOC}$ under visible light irradiation is proposed in Fig. 8b.

4. Conclusions

In summary, the nanocomposites of $\text{Bi}_2\text{S}_3/\text{Bi}_2\text{O}_3/\text{BOC}$ were successfully synthesized via combining the rational heat-treatment process and ion exchange technique. As reported here, these composites exhibit enhanced photocatalytic activities in organic

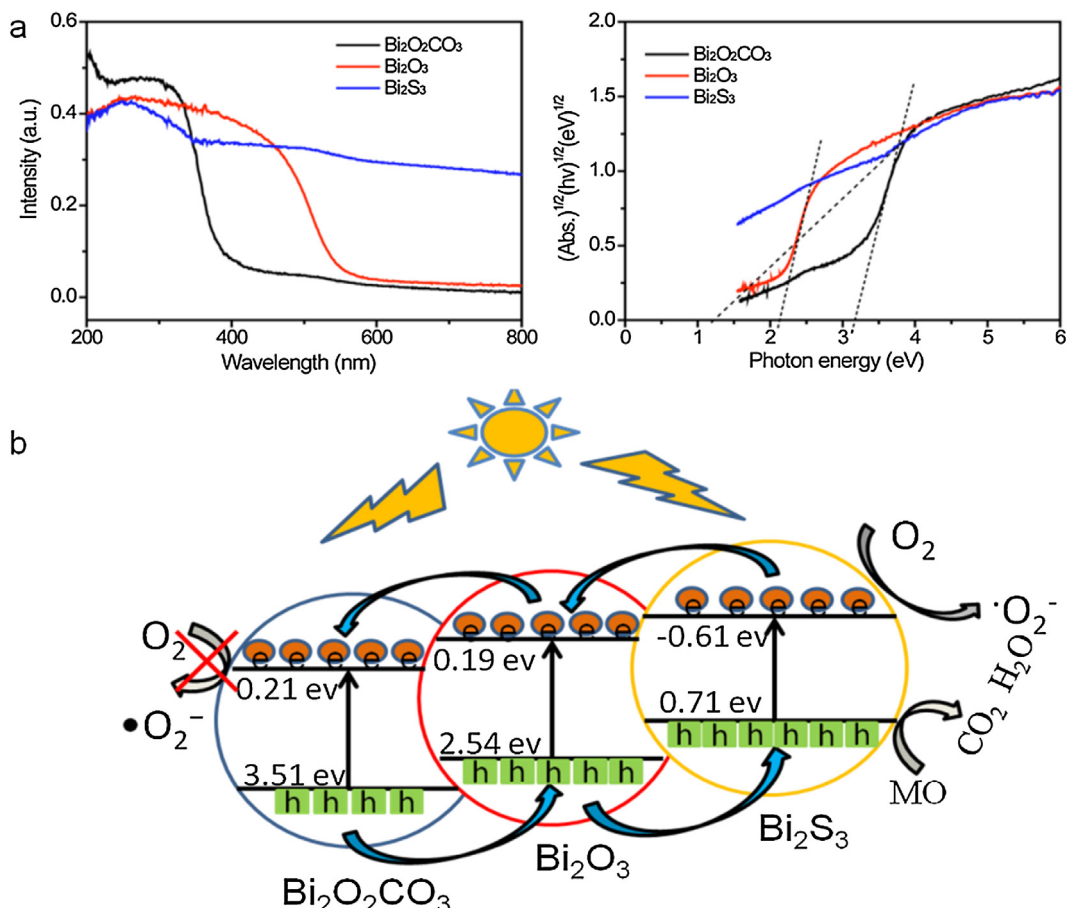


Fig. 8. (a) UV–vis absorption spectra and plots of the $(\alpha h\nu)^{1/2}$ vs photon energy ($h\nu$) of BOC, $\text{Bi}_2\text{O}_3/\text{BOC}$ and $\text{Bi}_2\text{S}_3/\text{Bi}_2\text{O}_3/\text{BOC}$. (b) A schematic diagram for the charge-transfer process in $\text{Bi}_2\text{S}_3/\text{Bi}_2\text{O}_3/\text{BOC}$ nanocomposites.

pollutants degradation under the visible light irradiation. The $\text{Bi}_2\text{S}_3/\text{Bi}_2\text{O}_3/\text{BOC}$ catalyst could eliminate 99% HCHO (500 ppm) in 100 min under visible light. Furthermore, it also could remove more than 99% of MO within 60 min, which is considerably higher than those of pure BOC (19.5%) and $\text{Bi}_2\text{O}_3/\text{BOC}$ (42.1%) samples at the same condition. Additionally, the $\text{Bi}_2\text{S}_3/\text{Bi}_2\text{O}_3/\text{BOC}$ has an excellent cycling stability after 5 cycles. The highly improved performance of the composites can be ascribed to the increased light absorption and efficient charge separation. The mechanism of the high photocatalytic activity demonstrated that the photocatalytic process is mainly governed by the superoxide and the holes rather than the hydroxyl radicals. This work provides a promising route to design other ideal Bi-based oxide hierarchical architectures for future application.

Acknowledgments

This work was supported by the Science and Technology Plan Project (2013B090600036), the Natural Science Foundation of China (21425627, 21461162003 and 21476271) and Natural Science Foundation (2014A030308012 and 2014KTSCX004) of Guangdong Province, China.

Appendix A. Supplementary data

Supplementary data associated with this article can be found, in the online version, at <http://dx.doi.org/10.1016/j.apcatb.2015.11.043>.

References

- [1] Q. Liu, J. He, T. Yao, Z. Sun, W. Cheng, S. He, Y. Xie, Y. Peng, H. Cheng, Y. Sun, *Nat. Commun.* 5 (2014), <http://dx.doi.org/10.1038/ncomms6122>.
- [2] H. Li, Y. Zhou, W. Tu, J. Ye, Z. Zou, *Adv. Funct. Mater.* 25 (2015) 998–1013.
- [3] Q. Li, X. Li, S. Wageh, A. Al-Ghamdi, J. Yu, *Adv. Energy Mater.* 5 (2015), <http://dx.doi.org/10.1002/aenm.201500010>.
- [4] H. Tong, S. Ouyang, Y. Bi, N. Umezawa, M. Oshikiri, J. Ye, *Adv. Mater.* 24 (2012) 229–251.
- [5] H. Cheng, B. Huang, Y. Dai, *Nanoscale* 6 (2014) 2009–2026.
- [6] Y. Huang, B. Long, H. Li, M.S. Balogun, Z. Rui, Y. Tong, H. Ji, *Adv. Mater. Interfaces* (2015), <http://dx.doi.org/10.1002/admi.201500249>.
- [7] M. Guan, C. Xiao, J. Zhang, S. Fan, R. An, Q. Cheng, J. Xie, M. Zhou, B. Ye, Y. Xie, *J. Am. Chem. Soc.* 135 (2013) 10411–10417.
- [8] Y. Ma, Y. Jia, Z. Jiao, M. Yang, Y. Qi, Y. Bi, *Chem. Commun.* 51 (2015) 6655–6658.
- [9] X. Chang, T. Wang, P. Zhang, J. Zhang, A. Li, J. Gong, *J. Am. Chem. Soc.* 137 (2015) 8356–8359.
- [10] L. Ye, J. Liu, C. Gong, L. Tian, T. Peng, L. Zan, *ACS Catal.* 2 (2012) 1677–1683.
- [11] G. Liu, T. Wang, S. Ouyang, L. Liu, H. Jiang, Q. Yu, T. Kako, J. Ye, *J. Mater. Chem. A* 3 (2015) 8123–8132.
- [12] F. Dong, Q. Li, Y. Sun, W.K. Ho, *ACS Catal.* 4 (2014) 4341–4350.
- [13] L. Chen, R. Huang, S.F. Yin, S.L. Luo, C.T. Au, *Chem. Eng. J.* 193 (2012) 123–130.
- [14] L. Chen, S.F. Yin, S.L. Luo, R. Huang, Q. Zhang, T. Hong, P.C. Au, *Ind. Eng. Chem. Res.* 51 (2012) 6760–6768.
- [15] T. Xiong, H. Huang, Y. Sun, F. Dong, *J. Mater. Chem. A* 3 (2015) 6118–6127.
- [16] F. Dong, Y. Sun, M. Fu, W.K. Ho, S.C. Lee, Z. Wu, *Langmuir* 28 (2011) 766–773.
- [17] H. Zhao, J. Tang, Q. Lai, G. Cheng, Y. Liu, R. Chen, *Catal. Commun.* 58 (2015) 190–194.
- [18] Z. Zhao, Y. Zhou, F. Wang, K. Zhang, S. Yu, K. Cao, *ACS Appl. Mater. Interfaces* 7 (2014) 730–737.
- [19] P. Madhusudan, J. Ran, J. Zhang, J. Yu, G. Liu, *Appl. Catal. B Environ.* 110 (2011) 286–295.
- [20] C. Li, G. Chen, J. Sun, Y. Feng, J. Liu, H. Dong, *Appl. Catal. B Environ.* 163 (2015) 415–423.
- [21] G. Cai, L. Xu, B. Wei, J. Che, H. Gao, W. Sun, *Mater. Lett.* 120 (2014) 1–4.
- [22] R. Hu, X. Xiao, S. Tu, X. Zuo, J. Nan, *Appl. Catal. B Environ.* 163 (2015) 510–519.
- [23] K.H. Ye, X. Yu, Z. Qiu, Y. Zhu, X. Lu, Y. Zhang, *RSC Adv.* 5 (2015) 34152–34156.

[24] T. Zhu, Y. Song, H. Ji, Y. Xu, Y. Song, J. Xia, S. Yin, Y. Li, H. Xu, Q. Zhang, H. Li, *Chem. Eng. J.* 271 (2015) 96–105.

[25] Z. Yu, B. Yin, F. Qu, X. Wu, *Chem. Eng. J.* 258 (2014) 203–209.

[26] J. Yu, J. Zhang, M. Jaroniec, *Green Chem.* 12 (2010) 1611–1614.

[27] G. Konstantatos, L. Levina, J. Tang, E.H. Sargent, *Nano Lett.* 8 (2008) 4002–4006.

[28] W. Xitao, L. Rong, W. Kang, *J. Mater. Chem. A* 2 (2014) 8304–8313.

[29] J.M. Hodges, K. Kletetschka, J.L. Fenton, C.G. Read, R.E. Schaak, *Angew. Chem. Int. Ed.* 54 (2015) 8669–8672.

[30] J.M. Pietryga, D.J. Werder, D.J. Williams, J.L. Casson, R.D. Schaller, V.I. Klimov, J.A. Hollingsworth, *J. Am. Chem. Soc.* 130 (2008) 4879–4885.

[31] Q.A. Akkerman, A. Genovese, C. George, M. Prato, I. Moreels, A. Casu, S. Marras, A. Curcio, A. Scarpellini, T. Pellegrino, *ACS Nano* 9 (2015) 521–531.

[32] N. Tian, H. Huang, Y. Guo, Y. He, Y. Zhang, *Appl. Surf. Sci.* 322 (2014) 249–254.

[33] O.C. Monteiro, H.I. Nogueira, T. Trindade, M. Motevali, *Chem. Mater.* 13 (2001) 2103–2111.

[34] P. Madhusudan, J. Yu, W. Wang, B. Cheng, G. Liu, *Dalton Trans.* 41 (2012) 14345–14353.

[35] Q. Han, J. Chen, X. Yang, L. Lu, X. Wang, *J. Phys. Chem. C* 111 (2007) 14072–14077.

[36] Y. Huang, H. Li, M.S. Balogun, W. Liu, Y. Tong, X. Lu, H. Ji, *ACS Appl. Mater. Interfaces* 6 (2014) 22920–22927.

[37] S. Shamaila, A.K.L. Sajjad, F. Chen, J. Zhang, *Appl. Catal. B Environ.* 94 (2010) 272–280.

[38] Y. Huang, H. Li, M.S. Balogun, H. Yang, Y. Tong, X. Lu, H. Ji, *RSC Adv.* 5 (2014) 7729–7733.

[39] Y. Huang, B. Long, M. Tang, Z. Rui, M.S. Balogun, Y. Tong, H. Ji, *Appl. Catal. B Environ.* 181 (2016) 779–787.

[40] K.H. Ye, Z. Chai, J. Gu, X. Yu, C. Zhao, Y. Zhang, W. Mai, *Nano Energy* (2015), <http://dx.doi.org/10.1016/j.nanoen.2015.10.018>.

[41] J. Tian, Y. Sang, Z. Zhao, W. Zhou, D. Wang, X. Kang, H. Liu, J. Wang, S. Chen, H. Cai, *Small* 9 (2013) 3864–3872.

[42] F. Lei, Y. Sun, K. Liu, S. Gao, L. Liang, B. Pan, Y. Xie, *J. Am. Chem. Soc.* 136 (2014) 6826–6829.

[43] Y.S. Xu, W.D. Zhang, *Appl. Catal. B Environ.* 140 (2013) 306–316.